LETTER TO THE EDITOR

Dense gas relations at kiloparsec scale across nearby galaxies with EMPIRE and ALMOND

Lukas Neumann[1],[*],[**] ⬤ , María J. Jiménez-Donaire[2,3] ⬤ , Frank Bigiel[1] ⬤ , Adam K. Leroy[4] ⬤ , Antonio Usero[2] ⬤ , Jiayi Sun[5] ⬤ , Eva Schinnerer[6] ⬤ , Miguel Querejeta[2] ⬤ , Sophia K. Stuber[6] ⬤ , Ivana Bešlić[7] ⬤ , and the PHANGS Team

(Affiliations can be found after the references)

ABSTRACT

Dense molecular gas is the key ingredient for star formation. Over the last two decades, HCN(1–0) emission has been extensively utilised to probe the dense, immediate star-forming gas from the Milky Way to external galaxies. In this work, we compile the largest resolved galaxy sample of HCN maps in the local universe ($d < 25$ Mpc) by merging and homogenising the EMPIRE and ALMOND surveys to investigate dense gas scaling relations in spiral galaxies at kiloparsec scales. We measure HCN/CO, a proxy for the dense gas fraction, and SFR/HCN, a proxy for the dense gas star formation efficiency, at kiloparsec scales across 31 galaxies and compare them with the molecular gas surface density, stellar mass surface density, and dynamical equilibrium pressure, adopting a best-effort, variable CO-to-H_2 conversion factor. We show that HCN/CO increases, while SFR/HCN decreases with the molecular gas surface density, stellar mass surface density and pressure, conditions typically found towards galaxy centres. We find that galaxy centres with high stellar mass surface density show a factor of a few higher HCN/CO and lower SFR/HCN compared to the disc average. In contrast, the presence of a bar or an active galactic nucleus does not significantly affect these ratios in centres. We conclude that EMPIRE and ALMOND yield consistent results and represent the most robust constraints on kiloparsec-scale scaling relations across nearby star-forming galaxies to date.

Key words. ISM: molecules – Galaxies: ISM – Galaxies: star formation

1. Introduction

Stars form from the coldest, densest substructures within molecular clouds. High-critical density molecular lines ("dense gas tracers") allow us to observe the subset of dense molecular gas directly linked to star formation, with the brightest and most commonly used extragalactic dense gas tracers being HCN(1 − 0) (hereafter HCN) and HCO^+(1 − 0). A nearly linear correlation has been observed between the star formation rate (SFR) and the dense gas tracer luminosity as traced by HCN emission across a wide range of scales (e.g., Gao & Solomon 2004; Wu et al. 2010; García-Burillo et al. 2012; Usero et al. 2015; Chen et al. 2017). This has been interpreted to indicate a significant and perhaps even universal role for dense gas in the star formation process. This, in turn, prompts the question "If the amount of dense gas controls the rate of star formation, what sets the amount of dense gas?" More, already in these early studies there have been suggestions that the rate of star formation per unit dense gas tracer luminosity or dense gas mass ($SFE_{dense} \equiv SFR/M_{dense}$) is not truly universal, but varies from galaxy-to-galaxy and location-to-location (García-Burillo et al. 2012; Usero et al. 2015; Chen et al. 2015).

Most early studies targeted either integrated galaxies, individual parts of galaxies, or selected star-forming clumps in the Milky Way. Therefore, a natural next step was to map the dense gas, total molecular gas, and star formation activity together across the whole area of diverse samples of star-forming galaxies. Over the last five years, the first systematic dense gas tracer mapping surveys that cover whole galaxies have emerged. The IRAM-30m large program EMPIRE[1] (Bigiel et al. 2016; Jiménez-Donaire et al. 2017, 2019) obtained ∼ kiloparsec-resolution maps of dense gas tracers (HCN, HCO^+, HNC(1 − 0)), and CO isotopologues for nine nearby galaxies. The ALMOND[2] survey (Neumann et al. 2023b) used the Morita Atacama Compact Array (ACA) to map HCN, HCO^+, and CS(2 − 1) emission from 25 nearby galaxies where CO(2 − 1) maps already exist from PHANGS–ALMA (Leroy et al. 2021a). Meanwhile, a number of smaller surveys have used ALMA or the IRAM telescopes to observe dense gas tracers in individual regions or small samples of 1−4 galaxies (Gallagher et al. 2018b,a; Querejeta et al. 2019; Bešlić et al. 2021; Heyer et al. 2022; Neumann et al. 2023b).

These mapping surveys confirmed significant variations in the observed dense gas tracer intensities, at face value implying variable star formation efficiency. The ratios of SFR/HCN (as a proxy for the star formation efficiency in dense gas) and HCN-to-CO (contrasting high and low critical density tracers) correlate with the local stellar and gas surface density, dynamical equilibrium pressure, and other environmental factors. These variations appear to have a regular sense, with denser gas (higher HCN/CO) and lower SFR/HCN in high surface density, high-pressure regions.

---

[1] Eight MIxing Receiver (EMIR) Multiline Probe of the Interstellar medium (ISM) Regulating galaxy Evolution; https://empiresurvey.yourwebsitespace.com
[2] ACA Large-sample Mapping Of Nearby galaxies in Dense gas.

This letter synthesizes the two largest HCN mapping surveys for disk galaxies, ALMOND and EMPIRE, to present a homogeneously measured set of kiloparsec-resolution scaling relations that connect star formation, dense gas, and total molecular gas to these local environmental quantities. As of the publication of this work, this sample comprises the largest survey of resolved, nearby galaxies where dense gas tracers have been mapped at kiloparsec scales.

2. Data & Methods

We use the HCN data presented for EMPIRE in Jiménez-Donaire et al. (2019) and ALMOND in Neumann et al. (2023b). We direct the reader to those papers for details on the observations and data processing. The two data sets are well-matched. The ALMOND maps have resolution 17″ to 22″ and rms noise ≈ 3 mK per 10 km s^{-1}, while EMPIRE has resolution 33″ and rms noise $1-2$ mK per 10 km s^{-1} and targets moderately closer galaxies.

Galaxy sample Combining EMPIRE and ALMOND yields 31 galaxies. NGC 628, 2903, and 4321 overlap between surveys and yield consistent results (see App. C for a comparison). To avoid duplicates, we employ the ALMOND data for the overlapping galaxies. Tab. E.1 lists the targets along with integrated galaxy properties, angular and physical resolutions of the HCN observations. We use the native angular resolution of the HCN observations, which span $\sim 1-2$ kpc physical scales. All of these galaxies are nearby ($d < 25$ Mpc), relatively face-on ($i < 75^o$), gas-rich, and actively star-forming (SFR $\sim 0.2 - 17\ M_\odot$ yr^{-1}).

Integrated intensity maps Following Neumann et al. (2023b), we convolve all supporting data sets (e.g., SFR, CO, and stellar mass maps) to the angular resolution of the HCN observations using the `PyStructure` package[3]. We sample all maps with a common half-beam spaced hexagonal grid and compute the integrated intensities of the HCN and CO lines by integrating over a velocity range determined by the extent of CO emission.

Conversion factors To compute the dense gas ratios HCN/CO and SFR/HCN, we use fixed conversion factors $\alpha_{\rm CO} \equiv M_{\rm mol}/L_{\rm CO} \equiv \Sigma_{\rm mol}/I_{\rm CO}$ and $\alpha_{\rm HCN} \equiv M_{\rm dense}/L_{\rm HCN} \equiv \Sigma_{\rm dense}/I_{\rm HCN}$, adopting a Milky Way based $\alpha_{\rm CO}^{\rm fix} = 4.35\ M_\odot$ pc^{-2} (K km s^{-1})$^{-1}$ (Bolatto et al. 2013) and an extragalactic based $\alpha_{\rm HCN} = 15\ M_\odot$ pc^{-2} (K km s^{-1})$^{-1}$ (Schinnerer & Leroy 2024). As a result, these measurements can be straightforwardly translated from physical quantities back into observed intensities (e.g., "dense gas fraction" corresponds to HCN/CO). Aside from aiming to remain "close to the observations," we do this because although significant progress has been made in understanding the CO-to-H$_2$ conversion factor, $\alpha_{\rm CO}$, (e.g., see Bolatto et al. 2013; Schinnerer & Leroy 2024) the environmental dependence (or even existence) of the HCN to dense gas conversion factor, $\alpha_{\rm HCN}$, remains unclear, with no obvious best prescription and significant likely covariance with $\alpha_{\rm CO}$ (see Usero et al. 2015).

Nevertheless, to leverage recent progress in understanding $\alpha_{\rm CO}$ variations, we employ a variable $\alpha_{\rm CO}$ (hereafter $\alpha_{\rm CO}^{\rm var}$) to compute the molecular gas surface density ($\Sigma_{\rm mol}$) and dynamical equilibrium pressure ($P_{\rm DE}$; see paragraphs below), adopting the prescription from (Schinnerer & Leroy 2024). The variable $\alpha_{\rm CO}^{\rm var}$

---

[3] https://github.com/jdenbrok/PyStructure

depends on metallicity an stellar mass surface density. Moreover, we employ the CO(2 − 1)/CO(1 − 0) line ratio calibration as a function of star formation rate surface density from Schinnerer & Leroy (2024) to convert PHANGS–ALMA CO(2 − 1) maps into CO(1 − 0) intensities for the ALMOND sample (EMPIRE already has CO(1 − 0) maps). See App. for more details on the variable conversion factor prescriptions.

Dense gas fraction and star formation efficiency We calculate the "dense gas fraction" as the ratio between dense and bulk molecular gas, $f_{\rm dense} \equiv M_{\rm dense}/M_{\rm mol}$. For $f_{\rm dense}$, we adopt fixed conversion factors so that $f_{\rm dense}$ depends directly on the observed line ratio HCN/CO:

$$f_{\rm dense} \approx 3.5 \left(\frac{I_{\rm HCN}}{\rm K\,km\,s^{-1}}\right)\left(\frac{I_{\rm CO}}{\rm K\,km\,s^{-1}}\right)^{-1} . \tag{1}$$

We also calculate the star formation efficiency of dense molecular gas as SFE$_{\rm dense} \equiv$ SFR/M$_{\rm dense}$, which expresses the rate at which stars form per unit dense gas (i.e., the inverse of the dense gas depletion time, $\tau_{\rm dep}^{\rm dense} = M_{\rm dense}/$SFR). Again, we adopt a fixed $\alpha_{\rm HCN}$ so that SFE$_{\rm dense}$ corresponds directly to the SFR-to-HCN intensity ratio via:

$$\left(\frac{\rm SFE_{\rm dense}}{\rm yr^{-1}}\right) \approx 6.7 \times 10^{-2} \left(\frac{\Sigma_{\rm SFR}}{M_\odot\,{\rm yr^{-1}\,pc^{-2}}}\right)\left(\frac{I_{\rm HCN}}{\rm K\,km\,s^{-1}}\right)^{-1} . \tag{2}$$

Star formation rate (SFR) We estimate kpc-scale SFR following the methodology of the original ALMOND paper (Neumann et al. 2023b), which uses a combination of infrared (IR) (22 μm) maps from WISE (Wright et al. 2010) and far-ultraviolet (FUV, 154 nm) maps from GALEX (Martin et al. 2005). These maps are taken from the z0MGS atlas and converted to SFR following the best FUV+22μm prescription in Leroy et al. (2019). EMPIRE originally employed *Spitzer* and *Herschel* IR measurements to estimate the SFR. For this work, we adopt the same methodology across EMPIRE and ALMOND, using the FUV+22μm based SFR maps across the full sample.

Stellar mass We estimate stellar mass surface density ($\Sigma_\star$) from *Spitzer* 3.6 μm observations (Sheth et al. 2010; Querejeta et al. 2021). We use the dust-corrected maps from (Querejeta et al. 2015) and adopt a mass-to-light ratio of $\Upsilon_\star = 0.6\ M_\odot\ L_\odot$.

Molecular gas surface density We compute the molecular gas surface density, $\Sigma_{\rm mol}$, adopting a variable $\alpha_{\rm CO}^{\rm var}$:

$$\left(\frac{\Sigma_{\rm mol}}{M_\odot\,{\rm pc^{-2}}}\right) = \alpha_{\rm CO}^{\rm var} \left(\frac{I_{\rm CO}}{\rm K\,km\,s^{-1}}\right) . \tag{3}$$

that depends on $\Sigma_\star$ and Z. We note that only $\Sigma_{\rm mol}$ and $P_{\rm DE}$ use a variable $\alpha_{\rm CO}$ (in contrast to $f_{\rm dense}$ and SFE$_{\rm dense}$, which use fixed conversion factors, $\alpha_{\rm CO}^{\rm fix}$, $\alpha_{\rm HCN}$).

Dynamical equilibrium pressure The dynamical equilibrium pressure ($P_{\rm DE}$) expresses the total interstellar pressure needed to support a disk in vertical dynamical equilibrium (e.g., see Ostriker & Kim 2022; Schinnerer & Leroy 2024). We estimate $P_{\rm DE}$ by calculating the weight of the ISM in the galaxy potential via:

$$P_{\rm DE} = \frac{\pi G}{2}\Sigma_{\rm gas}^2 + \Sigma_{\rm gas}\ \sqrt{2G\rho_\star}\ \sigma_{\rm gas,z} , \tag{4}$$
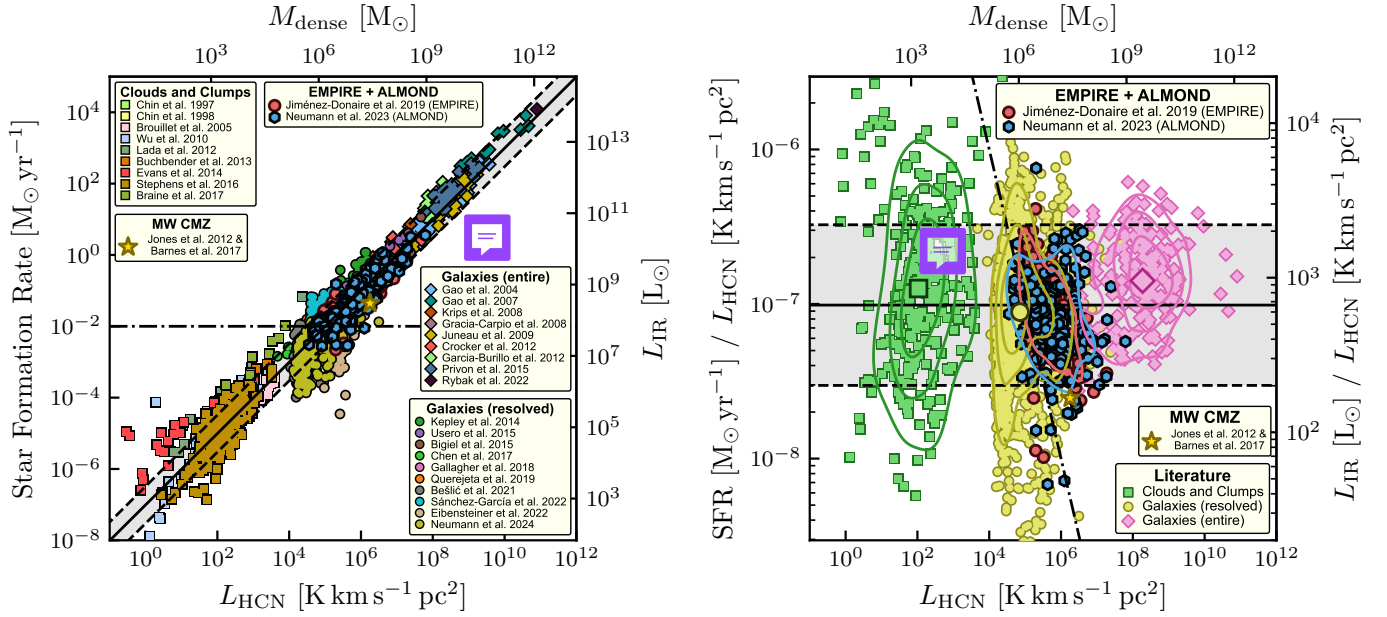
Fig. 1. Gao–Solomon relation. Star formation rate (SFR, left) and star formation efficiency (SFE$_{\mathrm{dense}}$, right) of dense gas as a function of the HCN luminosity, tracing dense gas mass across a literature compilation overlaid with data from EMPIRE (red circles; nine galaxies; Jiménez-Donaire et al. 2019) and ALMOND (blue hexagons; 25 galaxies; Neumann et al. 2023b). The black solid line shows the median SFR/HCN computed from detected sightlines across all data sets and the dashed lines mark the 1-sigma scatter (Tab. 1). The dash-dotted line in each panel marks the SFR threshold below which SFR estimates become more uncertain since resolved regions ≲ 500 pc do not average over large enough areas and timescales. Our literature compilation contains HCN observations that include Galactic clumps and clouds (squares), resolved nearby galaxies (circles) and unresolved entire galaxies (diamonds). More details on the respective targets are listed in Appendix B. In the right panel, these sub-samples are shown in green, olive, and pink, respectively, and are overlaid with 25, 50, and 75 percentile density contours. The red and blue contours present the 25 percentile levels of EMPIRE and ALMOND, respectively. The large markers (square, circle, diamond) indicate median values across the respective sub-samples.

where $\Sigma_{\mathrm{gas}} = \Sigma_{\mathrm{mol}} + \Sigma_{\mathrm{atom}}$ is the total gas surface density, $\rho_\star$ is the stellar mass volume density, and $\sigma_{\mathrm{gas},z}$ is the gas velocity dispersion perpendicular to the galactic disc. Computing $\rho_\star$ requires estimates of the stellar scale heights, which have been taken from S^{4}G (see Sun et al. 2022, for more details). Estimating P_{DE} additionally requires measurements of the atomic gas content, which have been taken from H I 21-cm line observation, available for 19 galaxies of our sample (Tab. E.1), hence limiting the analysis of P_{DE} relations to those 19 galaxies.

3. Results & Discussion

3.1. Gao–Solomon relation

In Fig. 1, we present the "Gao–Solomon" relation (Gao & Solomon 2004), the scaling relationship between SFR to L_{HCN}. The literature compilation comprises 31 HCN surveys that span from the Milky Way to the high-redshift universe and include observations of individual cores and molecular clouds within the Milky Way and the Local Group, spatially resolved maps of galaxies, and integrated galaxy data. On the x- and y-axes, we indicate both the observed luminosities (HCN and IR) and the inferred physical quantities (M_{dense} and SFR), assuming linear conversions with fixed conversion factors α_{HCN} and C_{IR}[4].

In the right panel of Fig. 1, the y-axis displays the ratio between SFR and L_{HCN}. Across the full literature sample, we

---

[4] All data here have observed HCN, but for the y-axis we adopt the best-estimate SFR and convert to equivalent L_{IR} using a constant IR-to-SFR conversion factor, $C_{\mathrm{IR}} = 1.48 \times 10^{-10}\,\mathrm{M_\odot\,yr^{-1}\,L_\odot^{-1}}$ (Murphy et al. 2011).

Table 1. Gao–Solomon relation

	SFR/HCN	IR/HCN	σ	$\tau_{\mathrm{dep}}^{\mathrm{dense}}$	$\epsilon_{\mathrm{ff}}^{\mathrm{dense}}$
Clouds and clumps	−6.90	2.93	0.70	8.08	−2.17
Resolved galaxies	−7.05	2.78	0.49	8.23	−2.32
Entire galaxies	−6.85	2.98	0.27	8.03	−2.12
Combined	−7.01	2.82	0.52	8.18	−2.28

Notes – Median dense gas ratios across the combined literature sample presented in Fig. 1, including EMPIRE and ALMOND, and for respective sub-samples, including clouds/clumps, resolved and integrated galaxy surveys. All values are displayed on a logarithmic scale. Columns 2 and 3 list the average SFR/HCN and IR/HCN in units of $\mathrm{M_\odot\,yr^{-1}/(K\,km\,s^{-1}\,pc^2)}$ and $\mathrm{L_\odot/(K\,km\,s^{-1}\,pc^2)}$, respectively. Column 4 shows the 1-sigma scatter (σ) of the detected HCN data around the median value. Columns 5 and 6 display the median dense gas depletion time ($\tau_{\mathrm{dep}}^{\mathrm{dense}}$, in units of years) and dense gas star formation efficiency per free-fall time ($\epsilon_{\mathrm{ff}}^{\mathrm{dense}}$), assuming HCN traces gas above $n_{\mathrm{H_2}}^{\mathrm{dense}} \approx 10^4\,\mathrm{cm^{-3}}$ and using $\alpha_{\mathrm{HCN}} = 15\,\mathrm{M_\odot\,pc^{-2}\,(K\,km\,s^{-1})^{-1}}$.

find a median SFR/HCN of $9.8 \times 10^{-8}\,\mathrm{M_\odot\,yr^{-1}\,(K\,km\,s^{-1}\,pc^2)^{-1}}$ with a 1-sigma scatter of 0.52 dex consistent with previous literature compilations (e.g., Jiménez-Donaire et al. 2019; Bešlić et al. 2024). We also compute the respective median SFE$_{\mathrm{dense}}$ values and scatter ranges for the individual sample regimes, i.e. clouds (square), resolved galaxy observations (circle), and entire galaxies (diamond). The values are listed in Tab. 1. Overall,

the literature compilation demonstrates that the HCN luminosity is a reasonable predictor of the SFR from cloud to galaxy scale across 10 orders of magnitude. However, at a given HCN luminosity, there is a significant scatter $\sigma \sim 0.5$ dex. Moreover, the scatter increases from large ($\sigma = 0.27$ dex) to small scales ($\sigma = 0.70$ dex), suggesting that there are significant variations of SFE_{dense} within galaxies (discussed in Sect. 3.2) that average out at integrated galaxy scales.

The dense gas star formation efficiency, SFE_{dense}, can be interpreted as the rate per unit mass at which dense molecular gas converts into stars. Across the detected sightlines of the full literature sample, we find a median $SFE_{dense} \approx 6.6 \times 10^{-9}$ yr^{-1}, or equivalently, a median dense gas depletion time of $\tau_{dep}^{dense} \approx 152$ Myr (1-sigma interval of $46 - 505$ Myr), indicating that the rate of present-day star formation would consume the available dense gas in this time period. For reference, this is ≈ 10 times lower than estimates for τ_{dep}^{mol}, the overall molecular gas depletion time in similar samples (Sun et al. 2023). The star formation efficiency per free-fall time, $\epsilon_{ff}^{dense} = SFE_{dense}/t_{ff}^{dense}$, is of theoretical interest (e.g., Krumholz & Thompson 2007; Federrath & Klessen 2012) because it captures the efficiency of star formation relative to the timescale expected for gravitational collapse, and so normalizes for density. The free-fall time of the dense molecular gas, $t_{ff}^{dense} = 4.4 \times 10^6 (n_{H_2}^{dense}/100)^{-0.5} = 0.8$ Myr, can be computed assuming that HCN traces gas above a density of $n_{H_2}^{dense} \approx 3 \times 10^3$ cm^{-3} (Jones et al. 2023; Bemis et al. 2024). Across the full literature sample, we obtain a median $\epsilon_{ff}^{dense} \approx 0.5\%$ (1-sigma interval of $0.16 - 1.7\%$), which suggests that only 0.5 % of the dense molecular gas is converted into stars. This demonstrates that even in the dense gas, star formation appears to be an extremely inefficient process.

The EMPIRE and ALMOND surveys cover HCN luminosities between $L_{HCN} = 10^4$ K km s^{-1} pc^2 and 10^8 K km s^{-1} pc^2 and SFRs between sfr $= 10^{-3}$ M$_\odot$ yr^{-1} and 1 M$_\odot$ yr^{-1}. Both data sets follow the overall Gao–Solomon relation and show a comparable scatter to the full literature sample. The resolution of $\sim$ kiloparsec is, on the one hand, high enough to resolve galaxies into discrete regions like centres, bars and spiral arms and is, on the other hand, coarse enough to average over large enough regions to yield robust SFR and SFE_{dense} measurements, not too strongly affected by the time evolution of individual regions (e.g., Kim et al. 2022). Based on this, we proceed to measure how f_{dense} and SFE_{dense} depend on environmental conditions in ALMOND and EMPIRE.

3.2. Dense gas relations with environment

Many previous works have found that HCN/CO and SFR/HCN are not constant within galaxies, but vary systematically with environmental factors, including stellar surface density ($\Sigma_\star$), molecular gas surface density (Σ_{mol}), and interstellar pressure inferred from dynamical equilibrium (P_{DE}) (Usero et al. 2015; Gallagher et al. 2018b; Jiménez-Donaire et al. 2019). In Fig. 2 we use the combined EMPIRE and ALMOND data to make the best measurement to date of the scaling relations relating HCN/CO and SFR/HCN to these environmental factors. To measure these relations, we spectrally stack the HCN(1 − 0) and CO(1 − 0) lines in bins of $\Sigma_\star$, Σ_{mol} and P_{DE} using `PyStacker`[5]. We use the CO data, which has much higher signal-to-noise than the HCN to determine the local mean reference velocity for the stacks (see Neumann et al. 2023a, and references therein for de-

Table 2. Dense gas scaling relations (environment)

$\log_{10}(Y)$	$\log_{10}(X)$	m (unc.)	$b^\dagger$ (unc.)	σ	Corr. (p)
HCN/CO	$\Sigma_\star$	0.54 (0.03)	−1.70 (0.01)	0.21	0.76 (7.4×10^{-83})
	Σ_{mol}	0.66 (0.04)	−1.77 (0.01)	0.23	0.77 (2.8×10^{-85})
	P_{DE}	0.46 (0.03)	−1.75 (0.01)	0.18	0.80 (5.5×10^{-64})
SFR/HCN	$\Sigma_\star$	−0.63 (0.04)	−7.04 (0.02)	0.33	−0.65 (3.1×10^{-56})
	Σ_{mol}	−0.76 (0.07)	−6.93 (0.03)	0.42	−0.59 (1.2×10^{-43})
	P_{DE}	−0.56 (0.06)	−7.03 (0.03)	0.38	−0.59 (3.3×10^{-28})

Notes – Fit parameters obtained via linear regression with `LinMix` to the data shown in Fig. 2. The parameters m, b and σ are the slope, intercept and scatter of the relation. Corr. (p) denotes the Pearson correlation coefficient with corresponding p–value. $\Sigma_\star$ and Σ_{mol} are given in units of pc^{-2}; and P_{DE} in k_B K cm^{-3}.
† Intercepts are given with respect to an x-axis offset of 2.4, 1.4, and 5.0 in logarithmic scale and aforementioned units for $\Sigma_\star$, Σ_{mol} and P_{DE}, respectively.

tails on the spectral stacking methodology; App. D presents the spectral stacks of HCN and CO). We construct stacked relations for each galaxy individually. For bins in which the stacks do not yield clear detections, we provide upper limits for HCN/CO and lower limits for SFR/HCN. We fit the combined set of stacks for all galaxies using a linear function of the form:

$$\log_{10} Y = b + m \cdot (\log_{10} X - x_0) , \tag{5}$$

where $X = \{\Sigma_\star, \Sigma_{mol}, P_{DE}\}$ and $Y = \{HCN/CO, SFR/HCN\}$ are the x- and y-axis variables, respectively. The slopes and intercepts are denoted as m and b, $x_0 = \{2.4, 1.4, 5.0\}$ is the x-axis offset so that the intercept is measured close to the median X value. The fitting is performed with the linear regression tool `LinMix`[6], which takes into account measurement uncertainties and censored data (see e.g. Neumann et al. 2023b, for more details on the fitting routine). The fit parameters are presented in Tab. 2.

We measure strong correlations between the stacked HCN/CO and all three environmental factors and similarly strong anti-correlations between SFR/HCN and the same factors. In other words, HCN/CO increases, while SFR/HCN decreases with $\Sigma_\star$, Σ_{mol}, P_{DE}. The slopes are significant, with both HCN/CO and SFR/HCN changing by ~ 1 dex across our sample and the variations well predicted by environmental factors. ALMOND and EMPIRE show highly consistent results despite using different telescopes, targeting different samples, and using different CO lines. Our best-fit relations are similar, though slightly steeper, to those reported by Jiménez-Donaire et al. (2019) but are now measured for a larger and more diverse sample of galaxies. The steeper slopes have two reasons: a) the ALMOND sample shows steeper trends, and (b) the inclusion of non-detections into the fitting routines yields $\sim 10\%$ steeper slopes. We observe a larger scatter across the full sample of 31 galaxies compared to the nine EMPIRE galaxies alone, suggesting that the more diverse sample captures a wider range of conditions not captured by the simple scaling relations.

Overall, these consistent, systematic variations of HCN/CO and SFR/HCN with the$\sim$ kiloparsec-scale environment, suggest that molecular clouds couple to the environment in which they are embedded. The enhanced HCN/CO in high-surface density, high-pressure environments indicate that deeper gravitational potentials and more abundant overall molecular gas lead to the

---
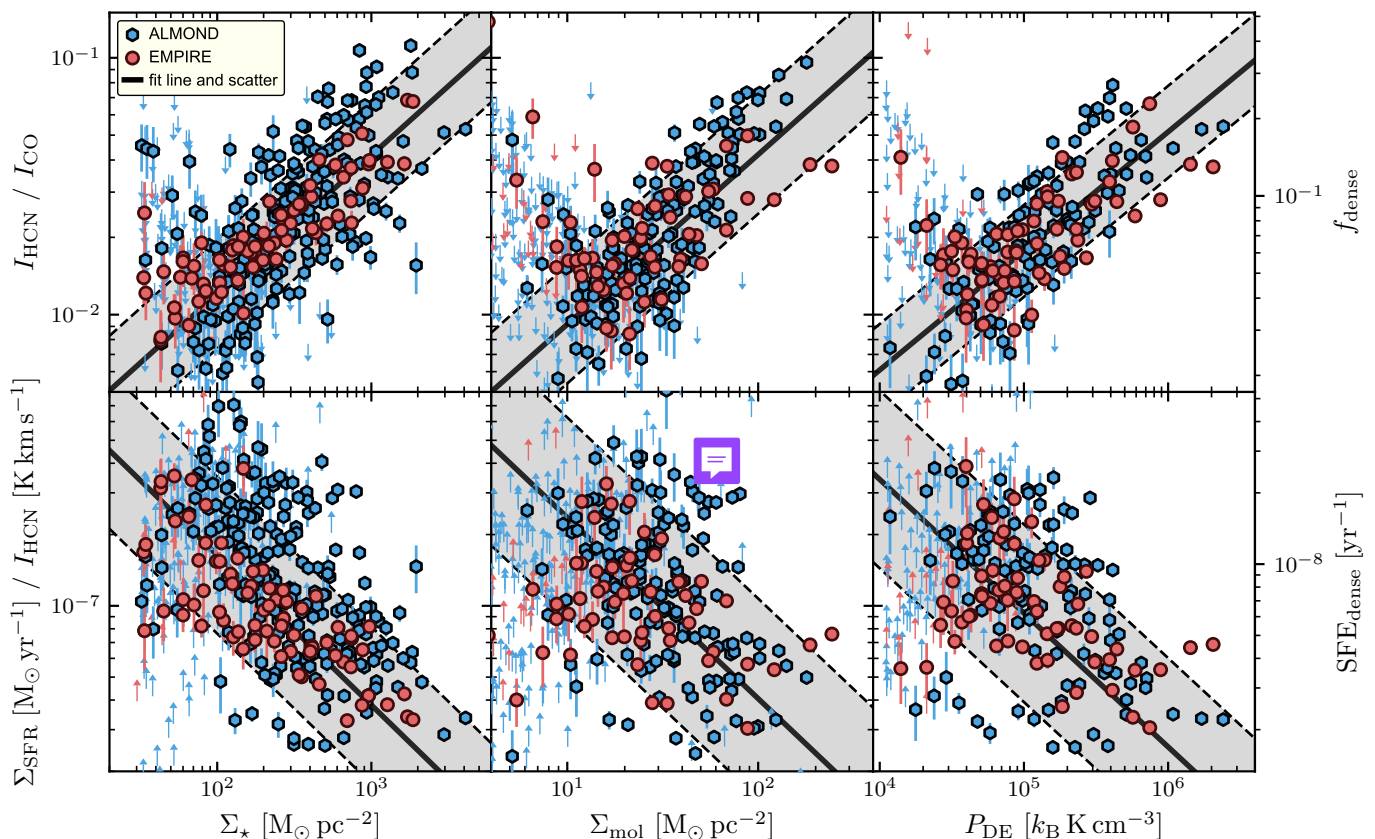
[5] https://github.com/PhangsTeam/PyStacker

[6] https://github.com/jmeyers314/linmix

Fig. 2. Dense gas relations with kiloparsec-scale environment. HCN/CO *(top)*, a proxy of f_{dense}, and SFR/HCN *(bottom)*, a proxy of $\text{SFE}_{\text{dense}}$, as a function of stellar mass surface density ($\Sigma_\star$), molecular gas surface density (Σ_{mol}), and dynamical equilibrium pressure (P_{DE}) across 31 galaxies from EMPIRE (red) and ALMOND (blue). The markers denote significant (S/N $\geq$ 3) stacked measurements and the downward and upward pointing arrows indicate upper (HCN/CO) and lower limits (SFR/HCN). All relations have been fitted with `LinMix` taking into account measurement uncertainties and upper/lower limits (parameters in Tab. 2). The black solid line shows the best fit line and the grey-shaded area indicates the 1-sigma scatter of the detected data.

formation of denser gas (a picture in good agreement with measurements of how cloud-scale mean gas properties depend on the environment Sun et al. 2022). Then, the specifically HCN-emitting molecular gas in these denser regions would be less efficiently converted into stars, plausibly because the material that emits HCN in these denser environments no longer uniquely corresponds to the overdense parts of clouds that collapse to form stars (a picture consistent turbulent cloud models, e.g., Krumholz & McKee 2005).

3.3. Dense gas ratios in galaxy centres

The centres of galaxies often exhibit high Σ_{mol}, $\Sigma_\star$, and P_{DE}, hence one expects high HCN/CO and low SFR/HCN in galaxy centres compared to the discs. In Fig. 3, we separately show the HCN/CO and SFR/HCN against $\Sigma_\star$ scaling relation (similar to the left panels of Fig. 2) for galaxy centres in contrast with measurements across the galaxy discs. Typically, galaxy centres are considered as the central few hundred parsecs of a galaxy (e.g. Querejeta et al. 2019). Across our data sets, which encompass kiloparsec scale measurements from EMPIRE and ALMOND, we consider the central beam size as the centre and refer to the remaining galaxy parts as the disc.

We find that centres typically have high HCN/CO (median of 0.013 compared to disc median of 0.045; Tab. E.2) and low SFR/HCN (median of 1.3×10^{-7} M$_\odot$ yr^{-1} pc^{-2} (K km s^{-1})$^{-1}$ com-

pared to disc median of 7.8×10^{-8} M$_\odot$ yr^{-1} pc^{-2} (K km s^{-1})$^{-1}$). Centres and discs show distinct distributions in the HCN/CO-$\Sigma_\star$ plane, where centres have a factor of 9 higher $\Sigma_\star$ and a factor of 3.5 higher HCN/CO. In the SFR/HCN-$\Sigma_\star$ relation, centres and discs have more comparable, overlapping SFR/HCN distributions with median values offset by a factor of 1.5. However, centres with particularly high $\Sigma_\star$ ($> 10^3$ M$_\odot$ pc^{-2}) show a factor of 2 lower SFR/HCN than discs. Such lower SFR/HCN is also observed for the CMZ of the Milky Way (Henshaw et al. 2023).

If taken at face value, the low SFR/HCN would imply that galaxy centres are typically less efficiently forming stars per unit of dense gas mass, which could be explained by higher gas turbulence in these environments acting against gravitational collapse (e.g., Usero et al. 2015; Neumann et al. 2023b). However, we emphasise that HCN might not be a robust tracer of dense gas in galaxy centres and we might expect that α_{HCN} varies between disc and centre regions, thus mitigating the interpretation of physical quantities like M_{dense} and $\text{SFE}_{\text{dense}}$ in galaxy centres. For instance, if one assumes that α_{HCN} variations are driven by optical depth effects and vary similarly to α_{CO} (Teng et al. 2023; Bemis et al. 2024), α_{HCN} would be lower in galaxy centres and thus yield higher $\text{SFE}_{\text{dense}}$ more comparable to disc values.

One might expect that active galactic nuclei (AGN) boost HCN emission (e.g., Goldsmith & Kauffmann 2018; Matsushita et al. 2015), deplete gas (e.g. Ellison et al. 2021), or quench SF (e.g., Nelson et al. 2019). Moreover, galactic bars have been re-
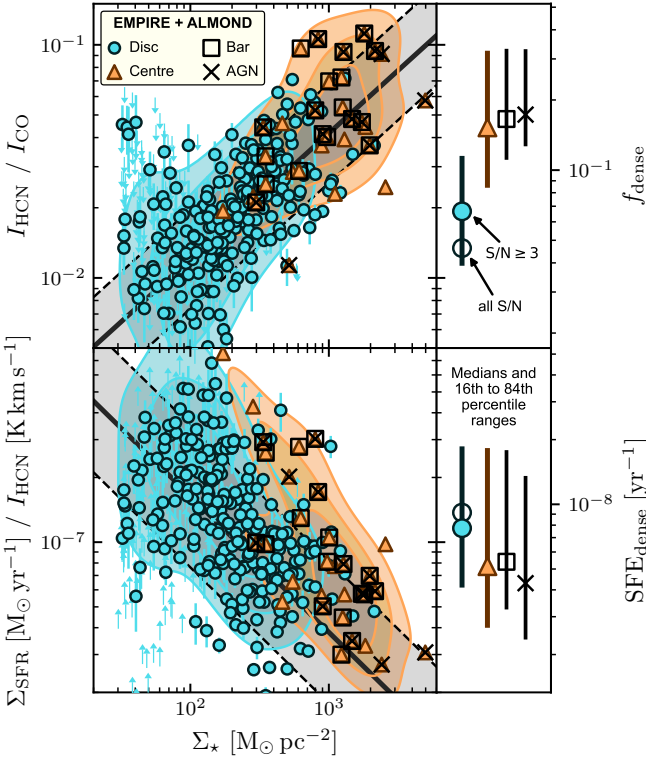
Fig. 3. Gao–Solomon relation for galaxy centres. Similar to the left panels of Fig. 2, but contrasting centre (orange triangles) and disc (cyan circles) measurements across the 31 galaxies from EMPIRE and ALMOND. The markers show detected data (S/N ≥ 3) and the filled contours indicate 25, 50 and 75 percentile areas across detections for disc (cyan) and centre (orange) measurements.

ported to show lower SFR/CO (e.g., Díaz-García et al. 2021; Maeda et al. 2023) and SFR/HCN (Neumann et al. 2024), suggesting lower star formation efficiencies in bar environments. In Fig. 3, we additionally indicate the presence of a bar (square; 19 galaxies) and an AGN (cross; 14 galaxies) for the galaxy centres and show their median and 1-sigma distributions in the right panels. The median values and distributions of HCN/CO and SFR/HCN in centres of barred or AGN galaxies are similar to those found in non-barred and non-AGN galaxies. Likely, the variations of dense gas and star formation between AGN-affected regions and bars are not well resolved at the scales (∼ 1 − 2 kpc) probed in this study.

4. Conclusions

We present state-of-the-art scaling relations relating the dense gas tracer HCN, SFR, and CO emission in star-forming disk galaxies. We particularly emphasize new measurements of kpc-scale scaling relations measured from 31 galaxies in the combined ALMOND (25 galaxies; Neumann et al. 2023b) and EMPIRE (6 galaxies; Jiménez-Donaire et al. 2019) data sets. Together these form the largest set of kpc resolution dense gas tracer maps of nearby (D < 25 Mpc) galaxies.

We place these data in the context of the Gao-Solomon relation which links SFR to L_{HCN}. We present an extensive compilation of data spanning from Milky Way cores to high-z and provide up-to-date estimates of the median and scatter of the SFR-to-HCN ratio in the literature. Galaxy regions in ALMOND

and EMPIRE lie in good agreement with these broader literature data.

We also show how SFR/CO, tracing the overall star formation efficiency of molecular, correlates with HCN/CO tracing the dense gas fraction. Meanwhile, SFR/HCN exhibits an anticorrelation with HCN/CO. Both HCN/CO and SFR/HCN vary systematically as a function of environment. HCN/CO increases and SFR/HCN decreases with stellar mass density ($\Sigma_\star$), molecular gas surface density (Σ_{mol}), and ISM pressure inferred from dynamical equilibrium (P_{DE}). We present scaling relations relating HCN/CO and SFR/HCN to Σ_{mol}, $\Sigma_\star$, and P_{DE}. ALMOND and EMPIRE yield consistent results and this work should represent the most robust, general constraints on these scaling relations to date.

Data availability

The HCN and CO data products used in this paper are publicly available via https://www.iram.fr/ILPA/LP015/ (EMPIRE), https://www.canfar.net/storage/list/phangs/RELEASES/ALMOND/ (ALMOND), and https://www.canfar.net/storage/list/phangs/RELEASES/PHANGS–ALMA/ (PHANGS–ALMA).

References

Anand, G. S., Lee, J. C., Van Dyk, S. D., et al. 2021, MNRAS, 501, 3621
Barnes, A. T., Longmore, S. N., Battersby, C., et al. 2017, MNRAS, 469, 2263
Bemis, A. R., Wilson, C. D., Sharda, P., Roberts, I. D., & He, H. 2024, arXiv e-prints, arXiv:2410.00243

Bešlić, I., Barnes, A. T., Bigiel, F., et al. 2024, A&A, 689, A122
Bešlić, I., Barnes, A. T., Bigiel, F., et al. 2021, MNRAS, 506, 963
Bigiel, F., Leroy, A. K., Blitz, L., et al. 2015, ApJ, 815, 103
Bigiel, F., Leroy, A. K., Jiménez-Donaire, M. J., et al. 2016, ApJ, 822, L26
Bolatto, A. D., Wolfire, M., & Leroy, A. K. 2013, ARA&A, 51, 207
Braine, J., Shimajiri, Y., André, P., et al. 2017, A&A, 597, A44
Brouillet, N., Muller, S., Herpin, F., Braine, J., & Jacq, T. 2005, A&A, 429, 153
Buchbender, C., Kramer, C., Gonzalez-Garcia, M., et al. 2013, A&A, 549, A17
Chen, H., Braine, J., Gao, Y., Koda, J., & Gu, Q. 2017, ApJ, 836, 101
Chen, H., Gao, Y., Braine, J., & Gu, Q. 2015, ApJ, 810, 140
Chin, Y. N., Henkel, C., Millar, T. J., Whiteoak, J. B., & Marx-Zimmer, M. 1998, A&A, 330, 901
Chin, Y. N., Henkel, C., Whiteoak, J. B., et al. 1997, A&A, 317, 548
Crocker, A., Krips, M., Bureau, M., et al. 2012, MNRAS, 421, 1298
den Brok, J. S., Chatzigiannakis, D., Bigiel, F., et al. 2021, MN-RAS[arXiv:2103.10442]
Díaz-García, S., Lisenfeld, U., Pérez, I., et al. 2021, A&A, 654, A135
Eibensteiner, C., Barnes, A. T., Bigiel, F., et al. 2022, A&A, 659, A173
Ellison, S. L., Wong, T., Sánchez, S. F., et al. 2021, MNRAS, 505, L46
Evans, Neal J., I., Heiderman, A., & Vutisalchavakul, N. 2014, ApJ, 782, 114
Federrath, C. & Klessen, R. S. 2012, ApJ, 761, 156
Gallagher, M. J., Leroy, A. K., Bigiel, F., et al. 2018a, ApJ, 868, L38
Gallagher, M. J., Leroy, A. K., Bigiel, F., et al. 2018b, ApJ, 858, 90
Gao, Y., Carilli, C. L., Solomon, P. M., & Vanden Bout, P. A. 2007, ApJ, 660, L93
Gao, Y. & Solomon, P. M. 2004, ApJ, 606, 271
García-Burillo, S., Usero, A., Alonso-Herrero, A., et al. 2012, A&A, 539, A8
Goldsmith, P. & Kauffmann, J. 2018, in American Astronomical Society Meeting Abstracts, Vol. 231, American Astronomical Society Meeting Abstracts #231, 130.06
Graciá-Carpio, J., García-Burillo, S., Planesas, P., Fuente, A., & Usero, A. 2008, A&A, 479, 703
Henshaw, J. D., Barnes, A. T., Battersby, C., et al. 2023, in Astronomical Society of the Pacific Conference Series, Vol. 534, Protostars and Planets VII, ed. S. Inutsuka, Y. Aikawa, T. Muto, K. Tomida, & M. Tamura, 83
Herrera-Endoqui, M., Díaz-García, S., Laurikainen, E., & Salo, H. 2015, A&A, 582, A86
Heyer, M., Gregg, B., Calzetti, D., et al. 2022, ApJ, 930, 170
Jiménez-Donaire, M. J., Bigiel, F., Leroy, A. K., et al. 2017, MNRAS, 466, 49
Jiménez-Donaire, M. J., Bigiel, F., Leroy, A. K., et al. 2019, ApJ, 880, 127
Jones, G. H., Clark, P. C., Glover, S. C. O., & Hacar, A. 2023, MNRAS, 520, 1005
Jones, P. A., Burton, M. G., Cunningham, M. R., et al. 2012, MNRAS, 419, 2961
Juneau, S., Narayanan, D. T., Moustakas, J., et al. 2009, ApJ, 707, 1217
Kepley, A. A., Leroy, A. K., Frayer, D., et al. 2014, ApJ, 780, L13
Kim, J., Chevance, M., Kruijssen, J. M. D., et al. 2022, MNRAS, 516, 3006
Krips, M., Neri, R., García-Burillo, S., et al. 2008, ApJ, 677, 262
Krumholz, M. R. & McKee, C. F. 2005, ApJ, 630, 250
Krumholz, M. R. & Thompson, T. A. 2007, ApJ, 669, 289
Lada, C. J., Forbrich, J., Lombardi, M., & Alves, J. F. 2012, ApJ, 745, 190
Lang, P., Meidt, S. E., Rosolowsky, E., et al. 2020, ApJ, 897, 122
Leroy, A. K., Hughes, A., Liu, D., et al. 2021a, ApJS, 255, 19
Leroy, A. K., Rosolowsky, E., Usero, A., et al. 2022, ApJ, 927, 149
Leroy, A. K., Sandstrom, K. M., Lang, D., et al. 2019, ApJS, 244, 24
Leroy, A. K., Schinnerer, E., Hughes, A., et al. 2021b, ApJS, 257, 43
Maeda, F., Egusa, F., Ohta, K., Fujimoto, Y., & Habe, A. 2023, ApJ, 943, 7
Martin, D. C., Fanson, J., Schiminovich, D., et al. 2005, ApJ, 619, L1
Matsushita, S., Trung, D.-V., Boone, F., et al. 2015, Publication of Korean Astronomical Society, 30, 439
Murphy, E. J., Condon, J. J., Schinnerer, E., et al. 2011, ApJ, 737, 67
Nelson, D., Pillepich, A., Springel, V., et al. 2019, MNRAS, 490, 3234
Neumann, L., Bigiel, F., Barnes, A. T., et al. 2024, arXiv e-prints, arXiv:2406.12025
Neumann, L., den Brok, J. S., Bigiel, F., et al. 2023a, A&A, 675, A104
Neumann, L., Gallagher, M. J., Bigiel, F., et al. 2023b, MNRAS, 521, 3348
Ostriker, E. C. & Kim, C.-G. 2022, ApJ, 936, 137
Privon, G. C., Herrero-Illana, R., Evans, A. S., et al. 2015, ApJ, 814, 39
Querejeta, M., Meidt, S. E., Schinnerer, E., et al. 2015, ApJS, 219, 5
Querejeta, M., Schinnerer, E., Meidt, S., et al. 2021, A&A, 656, A133
Querejeta, M., Schinnerer, E., Schruba, A., et al. 2019, A&A, 625, A19
Rybak, M., Hodge, J. A., Greve, T. R., et al. 2022, A&A, 667, A70
Sánchez, S. F., Barrera-Ballesteros, J. K., López-Cobá, C., et al. 2019, MNRAS, 484, 3042
Sánchez, S. F., Rosales-Ortega, F. F., Iglesias-Páramo, J., et al. 2014, A&A, 563, A49
Sánchez-García, M., García-Burillo, S., Pereira-Santaella, M., et al. 2022, A&A, 660, A83
Schinnerer, E. & Leroy, A. K. 2024, arXiv e-prints, arXiv:2403.19843
Sheth, K., Regan, M., Hinz, J. L., et al. 2010, PASP, 122, 1397
Stephens, I. W., Jackson, J. M., Whitaker, J. S., et al. 2016, ApJ, 824, 29

Sun, J., Leroy, A. K., Ostriker, E. C., et al. 2020, ApJ, 892, 148
Sun, J., Leroy, A. K., Ostriker, E. C., et al. 2023, ApJ, 945, L19
Sun, J., Leroy, A. K., Rosolowsky, E., et al. 2022, AJ, 164, 43
Teng, Y.-H., Sandstrom, K. M., Sun, J., et al. 2023, ApJ, 950, 119
Usero, A., Leroy, A. K., Walter, F., et al. 2015, AJ, 150, 115
Véron-Cetty, M. P. & Véron, P. 2010, A&A, 518, A10
Wright, E. L., Eisenhardt, P. R. M., Mainzer, A. K., et al. 2010, AJ, 140, 1868
Wu, J., Evans, Neal J., I., Shirley, Y. L., & Knez, C. 2010, ApJS, 188, 313

[1] Argelander-Institut für Astronomie, Universität Bonn, Auf dem Hügel 71, 53121 Bonn, Germany

[2] Observatorio Astronómico Nacional (IGN), C/ Alfonso XII, 3, E-28014 Madrid, Spain

[3] Centro de Desarrollos Tecnológicos, Observatorio de Yebes (IGN), 19141 Yebes, Guadalajara, Spain

[4] Department of Astronomy, The Ohio State University, 140 West 18th Ave, Columbus, OH 43210, USA

[5] Department of Astrophysical Sciences, Princeton University, 4 Ivy Lane, Princeton, NJ 08544, USA

[6] Max Planck Institute for Astronomy, Königstuhl 17, 69117 Heidelberg, Germany

[7] LERMA, Observatoire de Paris, PSL Research University, CNRS, Sorbonne Universités, 75014 Paris, France

Appendix A: Convsersion factors

For EMPIRE, we use the $CO(1-0)$ maps obtained as part of the survey. For ALMOND, we use PHANGS–ALMA $CO(2-1)$ maps, which we convert to an equivalent $CO(1-0)$ intensity before applying α_{CO}. To do this, we estimate a line ratio, R_{21}, based on the local SFR surface density (Σ_{SFR}) following den Brok et al. (2021); Leroy et al. (2022); Schinnerer & Leroy (2024):

$$R_{21} = \frac{CO(2-1)}{CO(1-0)} = 0.65 \left(\frac{\Sigma_{SFR}}{1.8 \times 10^{-2} \, M_\odot \, yr^{-1} \, kpc^{-2}} \right)^{0.125} , \tag{A.1}$$

with minimum R_{21} of 0.35 and maximum 1.0. Then we scale the $CO(2-1)$ intensity by R_{21}^{-1} to present our results in terms of $CO(1-0)$ intensity.

To compute Σ_{mol} and P_{DE}, we adopt the variable α_{CO} prescription from (Schinnerer & Leroy 2024) (their table 1), which accounts for variations with metallicity (Z; $Z_\odot$ is the solar metallicity) and stellar mass surface density ($\Sigma_\star$):

$$\alpha_{CO}^{var} = \alpha_{CO}^{fix} \left(\frac{Z}{Z_\odot} \right)^{-1.5} \left(\frac{\max(\Sigma_\star, 100 \, M_\odot \, pc^{-2})}{100 \, M_\odot \, pc^{-2}} \right)^{-0.25} . \tag{A.2}$$

Stellar mass maps are inferred from *Spitzer* 3.6 μm observations as explained in Sect. 2. Metallicities are estimated based on simple scaling relations, following (Sun et al. 2020). These use a global mass-metallicity relation (Sánchez et al. 2019) and employ a radial metallicity relation with a fixed gradient of -0.1 dex normalised by the effective radius of each galaxy (Sánchez et al. 2014).

Appendix B: Dense gas literature

In Fig. 1, we present a literature compilation of HCN surveys from local parsec scale over resolved, kiloparsec scale, to unresolved, entire galaxy observations. The cloud- and clump-scale measurements are taken from observations within the Milky Way (Wu et al. 2010; Lada et al. 2012; Evans et al. 2014; Stephens et al. 2016), the CMZ (Jones et al. 2012; Barnes et al. 2017) and the Local Group, i.e. LMC/SMC (Chin et al. 1997, 1998), M31 (Brouillet et al. 2005), M33 (Buchbender et al. 2013), low-metallicity local group galaxies (Braine et al. 2017). Resolved galaxy observations, typically from nearby galaxies at 100 pc to 2 kiloparsec scales, include M82 (Kepley et al. 2014), M51 (Usero et al. 2015; Chen et al. 2017; Querejeta et al. 2019), NGC 4038/39 (Bigiel et al. 2015), NGC 3351, NGC 3627, NGC 4254, NGC 4321, NGC 5194 (Gallagher et al. 2018b), NGC 3627 (Bešlić et al. 2021), NGC 1068 (Sánchez-García et al. 2022), NGC 6946 (Eibensteiner et al. 2022), NGC 4321 (Neumann et al. 2024), and the two larger-sample surveys EMPIRE (nine galaxies; Jiménez-Donaire et al. 2019) and ALMOND (25 galaxies; Neumann et al. 2023b). Integrated-galaxy data cover LIRG/ULIRG and AGN galaxies (Krips et al. 2008; Graciá-Carpio et al. 2008; Juneau et al. 2009; García-Burillo et al. 2012; Privon et al. 2015), early-type galaxies (Crocker et al. 2012), and high-redshift galaxies (Gao et al. 2007; Rybak et al. 2022).

Appendix C: EMPIRE vs ALMOND

There are three galaxies (i.e. NGC 628, NGC 2903, NGC 4321) that have been mapped in dense gas tracers (e.g. $HCN(1-0)$) by both surveys, EMPIRE, using the IRAM 30 m, and ALMOND,

using the ACA at similar spectral (a few km s^{-1}) and angular resolution (a few tenths of arcseconds) and sensitivity (a few mK). In Figures C.1 to C.3, we compare the $HCN(1-0)$ data from both surveys. We homogenise the two data sets by convolving to the best common spectral (i.e. 10 km s^{-1}) and spatial (i.e. 33″) resolution and reproject to the same half-beam size hexagonal pixel grid.

Fig. C.1 shows average $HCN(1-0)$ spectra computed across all sightlines within 5 kpc from the galactic centre. We additional overlay $CO(2-1)$ average spectra obtained from PHANGS–ALMA (Leroy et al. 2021b), to indicate molecular line emission from a highly significant tracer. This line has been used to infer the velocity-integration window from which we compute $HCN(1-0)$ integrated intensities of 41.6 ± 7.3 K km s^{-1}, 39.5 ± 10.7 K km s^{-1} in NGC 628, 427.8 ± 47.5 K km s^{-1}, 495.7 ± 143.5 K km s^{-1} in NGC 2903, and 475.0 ± 34.6 K km s^{-1}, 570.2 ± 84.8 K km s^{-1} in NGC 4321 from ALMOND and EMPIRE, respectively. The average spectra show similar shape and amplitude, demonstrating little to no bias between ALMOND and EMPIRE observations. The integrated line intensities yield consistent values within their uncertainties. The largest deviations are observed at large velocity offsets from the galaxies' systemtic velocities, potentially linked to poor baseline subtraction.

Fig. C.2 and C.3 present a voxel-by-voxel, or pixel-by-pixel comparison between the ALMOND and EMPIRE $HCN(1-0)$ brightness temperatures (ppv cube) and integrated intensities (moment-0 map). We find that brightness temperatures and integrated intensities agree well between ALMOND and EMPIRE in all galaxies (deviations ≤ 50 across most detected sightlines) and show little bias ($\leq 10\%$ on average across all data). At lower integrated intensities ($\lesssim 10^{-1}$ K km s^{-1}), EMPIRE yields moderately larger values than ALMOND, which could indicate differences in the calibration and data reduction pipelines.

The comparison between ALMOND and EMPIRE demonstrated that both data sets yield consistent $HCN(1-0)$ intensities and subsequent data products. In this work, we employ the ALMOND data for the three galaxies NGC 628, NGC 2903, NGC 4321, due to the slightly better angular resolution and sensitivity of the ALMOND survey.

Appendix D: Spectral stacking of HCN and CO

Figures D.1 to D.5 present stacked spectra of and $CO(1-0)$ line emission computed in bins of stellar mass surface density, $\Sigma_\star$ across all 31 galaxies studied in this work. For the ALMOND sample, the $CO(2-1)$ intensities from PHANGS–ALMA are first converted into $CO(1-0)$ intensities using the line ratio calibration from Sect. A (this has, however, no effect on the stacking procedure) These stacks are exemplary for all spectral stacks obtained in this work (we also compute stacks in Σ_{mol} and P_{DE} bins that are not shown here).

Appendix E: Additional figures/tables

Tab. E.1 presents the combined galaxy sample composed of 31 galaxies from the EMPIRE and ALMOND surveys, along with their coordinates and global properties.

Fig. E.1 shows the distribution of galaxies in the SFR against plane across PHANGS, EMPIRE and ALMOND galaxies. The two dense gas surveys (EMPIRE and ALMOND) utilised in this study encompass massive, actively star-forming galaxies with high SFR/, mostly lying above the star-forming main sequence.

Tab. E.2 lists percentile and median HCN/CO and SFR/HCN values for centre and discs environments discussed in Sec. 3.3.

Table E.1. Galaxy sample (EMPIRE + ALMOND)

Galaxy	R.A. (J2000)	Dec. (J2000)	d (Mpc)	i (°)	$\log_{10} M_\star$ (M$_\odot$)	$\log_{10}$ SFR (M$_\odot$ yr^{-1})	$\log_{10} (\text{SFR}/M_\star)$ (yr^{-1})	Bar	AGN	H I data	ALMOND	EMPIRE	Resolution ('')	(kpc)
(1)	(2)	(3)	(4)	(5)	(6)	(7)	(8)	(9)	(10)	(11)	(12)	(13)	(14)	(15)
NGC 0628	1ʰ36ᵐ41.7ˢ	15°47′1.1″	9.8	8.9	10.34	0.24	-10.10	✗	✗	✓	✓	✓	18.6	0.89
NGC 1097	2ʰ46ᵐ18.9ˢ	−30°16′28.8″	13.6	48.6	10.76	0.68	-10.08	✓	✓	✗	✓	✗	19.4	1.28
NGC 1365	3ʰ33ᵐ36.4ˢ	−36°8′25.5″	19.6	55.4	10.99	1.23	-9.76	✓	✓	✗	✓	✗	20.6	1.95
NGC 1385	3ʰ37ᵐ28.6ˢ	−24°30′4.2″	17.2	44.0	9.98	0.32	-9.66	✗	✗	✓	✓	✗	19.9	1.66
NGC 1511	3ʰ59ᵐ36.6ˢ	−67°38′2.1″	15.3	72.7	9.91	0.36	-9.55	✗	✗	✗	✓	✗	17.6	1.30
NGC 1546	4ʰ14ᵐ36.3ˢ	−56°3′39.2″	17.7	70.3	10.35	-0.08	-10.43	✗	✗	✗	✓	✗	18.9	1.62
NGC 1566	4ʰ20ᵐ0.4ˢ	−54°56′16.8″	17.7	29.5	10.78	0.66	-10.13	✓	✓	✗	✓	✗	19.7	1.69
NGC 1672	4ʰ45ᵐ42.5ˢ	−59°14′50.1″	19.4	42.6	10.73	0.88	-9.85	✓	✓	✗	✓	✗	18.2	1.71
NGC 1792	5ʰ5ᵐ14.3ˢ	−37°58′50.0″	16.2	65.1	10.61	0.57	-10.04	✗	✗	✗	✓	✗	18.7	1.47
NGC 2566	8ʰ18ᵐ45.6ˢ	−25°29′58.3″	23.4	48.5	10.71	0.94	-9.77	✓	✗	✓	✓	✗	18.5	2.10
NGC 2903	9ʰ32ᵐ10.1ˢ	21°30′3.0″	10.0	66.8	10.63	0.49	-10.15	✓	✗	✓	✓	✓	18.3	0.89
NGC 2997	9ʰ45ᵐ38.8ˢ	−31°11′27.9″	14.1	33.0	10.73	0.64	-10.09	✗	✗	✓	✓	✗	20.4	1.39
NGC 3059	9ʰ50ᵐ8.2ˢ	−73°55′19.9″	20.2	29.4	10.38	0.38	-10.00	✓	✗	✗	✓	✗	16.7	1.64
NGC 3184	10ʰ18ᵐ16.9ˢ	41°25′27.6″	12.6	16.0	10.36	0.11	-10.24	✓	✓	✓	✗	✓	33.3	2.03
NGC 3521	11ʰ5ᵐ48.6ˢ	0°2′9.4″	13.2	68.8	11.02	0.57	-10.45	✗	✗	✓	✓	✗	21.1	1.35
NGC 3621	11ʰ18ᵐ16.3ˢ	−32°48′45.4″	7.1	65.4	10.06	-0.00	-10.06	✗	✓	✓	✓	✗	18.9	0.65
NGC 3627	11ʰ20ᵐ15.0ˢ	12°59′29.4″	11.3	57.3	10.83	0.58	-10.25	✓	✓	✓	✗	✓	33.3	1.83
NGC 4254	12ʰ18ᵐ49.6ˢ	14°24′59.1″	13.1	34.4	10.42	0.49	-9.94	✗	✗	✓	✗	✓	33.3	2.11
NGC 4303	12ʰ21ᵐ54.9ˢ	4°28′25.5″	17.0	23.5	10.52	0.73	-9.80	✓	✓	✓	✓	✗	20.2	1.66
NGC 4321	12ʰ22ᵐ54.9ˢ	15°49′20.3″	15.2	38.5	10.75	0.55	-10.19	✓	✗	✓	✓	✓	19.6	1.45
NGC 4535	12ʰ34ᵐ20.3ˢ	8°11′52.7″	15.8	44.7	10.53	0.33	-10.20	✓	✗	✓	✓	✗	22.8	1.74
NGC 4536	12ʰ34ᵐ27.1ˢ	2°11′17.7″	16.2	66.0	10.40	0.54	-9.86	✓	✗	✓	✓	✗	21.5	1.69
NGC 4569	12ʰ36ᵐ49.8ˢ	13°9′46.4″	15.8	70.0	10.81	0.12	-10.68	✓	✓	✓	✓	✗	19.2	1.47
NGC 4826	12ʰ56ᵐ43.6ˢ	21°40′59.1″	4.4	59.1	10.24	-0.69	-10.93	✗	✓	✓	✓	✗	18.7	0.40
NGC 5055	13ʰ15ᵐ49.3ˢ	42°1′45.4″	9.0	59.0	10.79	0.31	-10.48	✗	✗	✓	✗	✓	33.3	1.46
NGC 5194	13ʰ29ᵐ52.7ˢ	47°11′42.5″	8.6	21.0	10.65	0.64	-10.01	✗	✓	✓	✗	✓	33.3	1.38
NGC 5248	13ʰ37ᵐ32.0ˢ	8°53′6.7″	14.9	47.4	10.41	0.36	-10.05	✓	✗	✓	✓	✗	19.9	1.43
NGC 5643	14ʰ32ᵐ40.8ˢ	−44°10′28.6″	12.7	29.9	10.34	0.41	-9.92	✓	✓	✗	✓	✗	18.0	1.11
NGC 6300	17ʰ16ᵐ59.5ˢ	−62°49′14.0″	11.6	49.6	10.47	0.28	-10.19	✓	✓	✗	✓	✗	17.7	0.99
NGC 6946	20ʰ34ᵐ52.6ˢ	60°9′12.7″	7.3	33.0	10.47	0.77	-9.70	✓	✗	✓	✗	✓	33.3	1.18
NGC 7496	23ʰ9ᵐ47.3ˢ	−43°25′40.3″	18.7	35.9	10.00	0.35	-9.64	✓	✓	✗	✓	✗	17.9	1.62

Notes – (2) Right ascension, (3) declination, (4) distance (Anand et al. 2021), and (5) inclination angle (Lang et al. 2020). Integrated galaxy properties, (6) global stellar mass and (7) global star formation rate, taken from Leroy et al. (2019). (9) Presence of a galactic bar (Herrera-Endoqui et al. 2015; Querejeta et al. 2021), and/or (10) active galactic nucleus (Véron-Cetty & Véron 2010). (11) Availability of archival H I 21-cm line emission data. (12) ALMOND (Neumann et al. 2023b) and (13) EMPIRE (Jiménez-Donaire et al. 2019) survey coverage. (14) Native angular resolution and (15) corresponding linear resolution, given the distance d.

Table E.2. Galaxy centres vs. discs

$\log_{10}(Y)$	environment	16ᵗʰ perc.	median	84ᵗʰ perc.	median (all S/N)
HCN/CO	disc	−1.94	−1.71	−1.49	−1.87
	centre	−1.60	−1.35	−1.04	−1.35
	centre (bar)	−1.49	−1.32	−1.03	−1.32
	centre (AGN)	−1.43	−1.30	−1.03	−1.28
SFR/HCN	disc	−7.20	−6.94	−6.57	−6.86
	centre	−7.39	−7.13	−6.57	−7.11
	centre (bar)	−7.30	−7.09	−6.58	−7.09
	centre (AGN)	−7.44	−7.19	−6.70	−7.23

Notes – 16ᵗʰ percentile, median, and 84ᵗʰ percentile of HCN/CO and SFR/HCN across significant data (S/N ≥ 3) in disc and centre environments. For the centres, we also present percentile values among centres with galactic bars and AGNs. The last column additionally lists the median values across all S/N data, this means including non-detections.
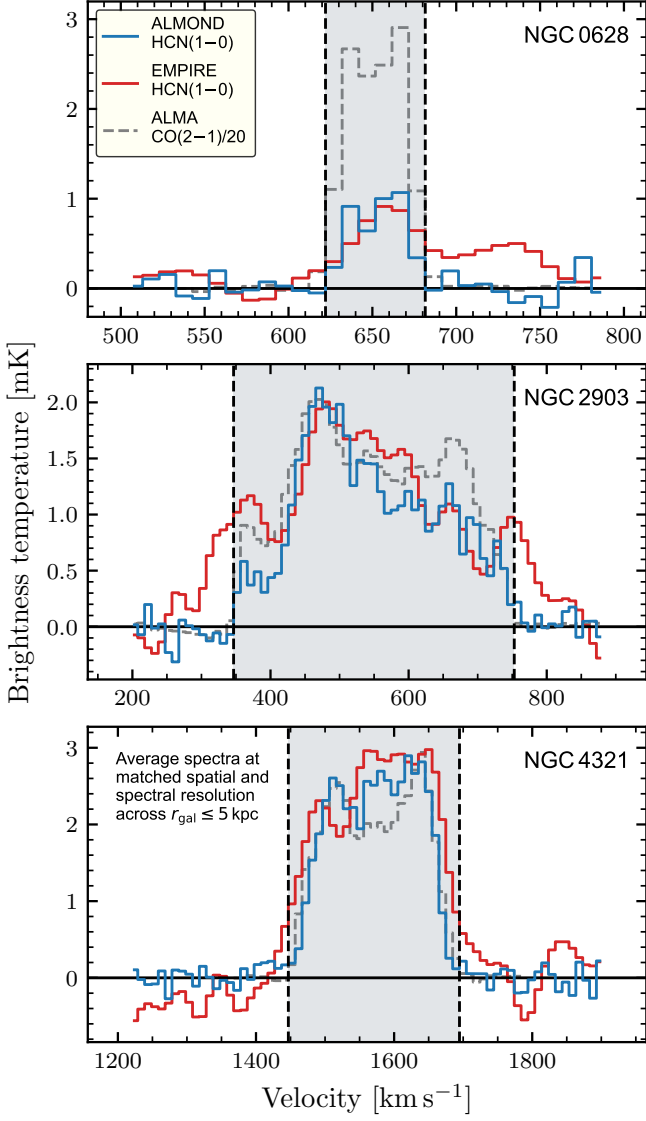
Fig. C.1. EMPIRE versus ALMOND: HCN(1 − 0) average spectra. The blue and red lines show average HCN brightness temperatures within $r_{\rm gal} \leq 5$ kpc obtained from spatially and spectrally matched ALMOND and EMPIRE observations, respectively, across the three galaxies NGC 628, NGC 2903, NGC 4321 from top to bottom. The grey dashed line shows (homogenised) CO(2 − 1) intensities from PHANGS–ALMA (Leroy et al. 2021b), scaled down by a factor of 20. The grey-shaded area indicates the velocity-integration window constructed using the highly significant CO(2 − 1) data. The resulting integrated intensities are quoted in the text.
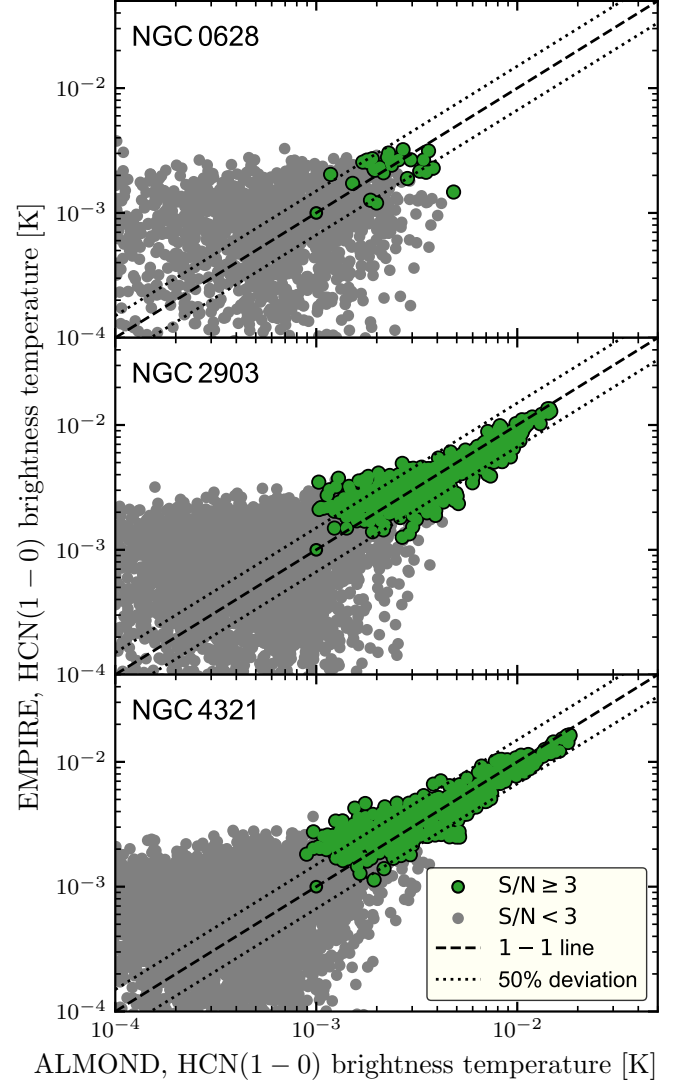
Fig. C.2. EMPIRE versus ALMOND: HCN(1 − 0) brightness temperature. Green data points present data, where EMPIRE and ALMOND both yield a 3-sigma detection. Grey data shows low-significant data points. The dashed line marks the 1-to-1 relation, where the dotted lines indicate a ±50 % deviation.
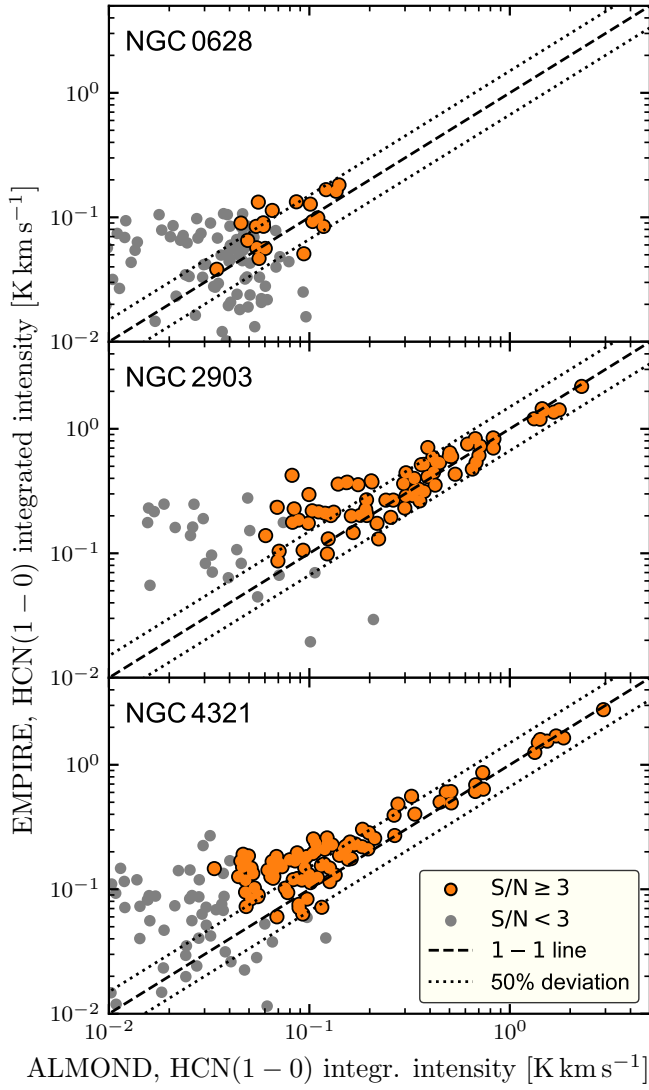
Fig. C.3. EMPIRE versus ALMOND: HCN(1 − 0) integrated intensity. Similar to Fig. C.2, but showing the integrated intensities (moment-o) computed across a CO-inferred velocity integration window. Orange and grey points denote data above and below 3-sigma, respectively.
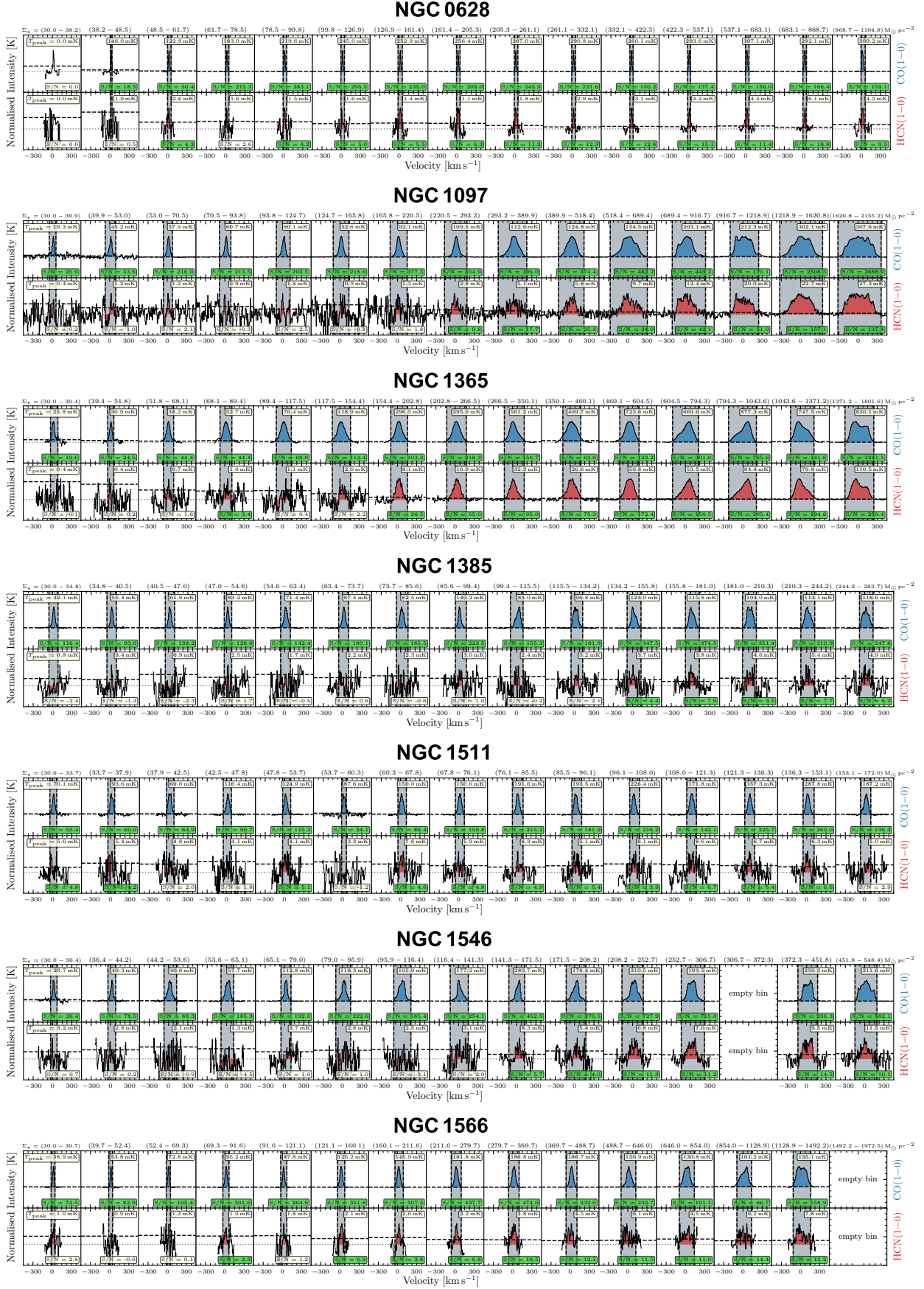
NGC 0628

NGC 1097

NGC 1365

NGC 1385

NGC 1511

NGC 1546

NGC 1566

Fig. D.1. Spectral stacks of CO (blue) and HCN (red) in logarithmically spaced $\Sigma_\star$ bins. The grey-shaded area indicates the velocity-integration window. The labels at the top and bottom of each panel show the peak brightness temperature and signal-to-noise ratio of each respective stacked spectrum, where detected spectra (S/N $\geq$ 3 are highlighted with a green box.
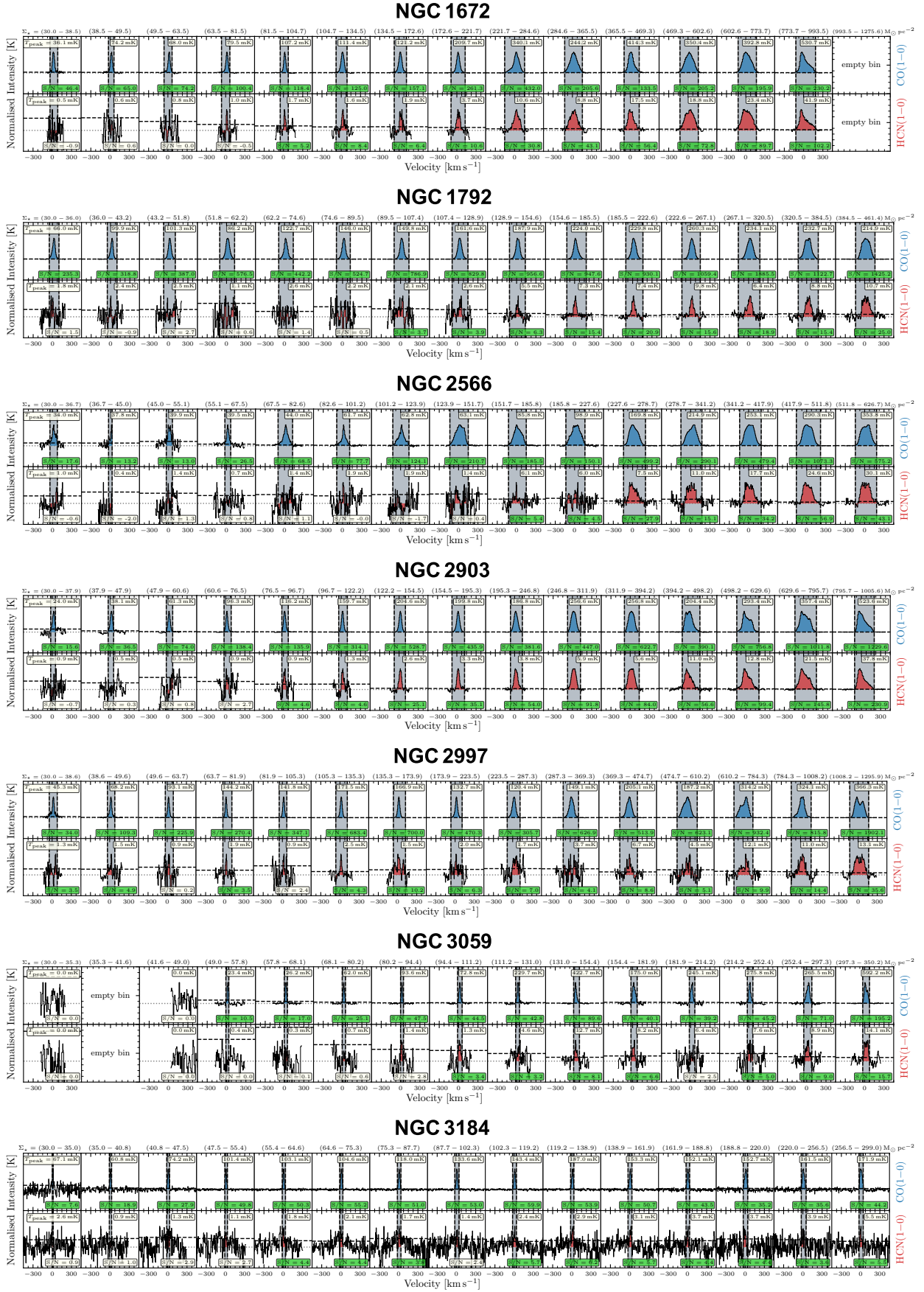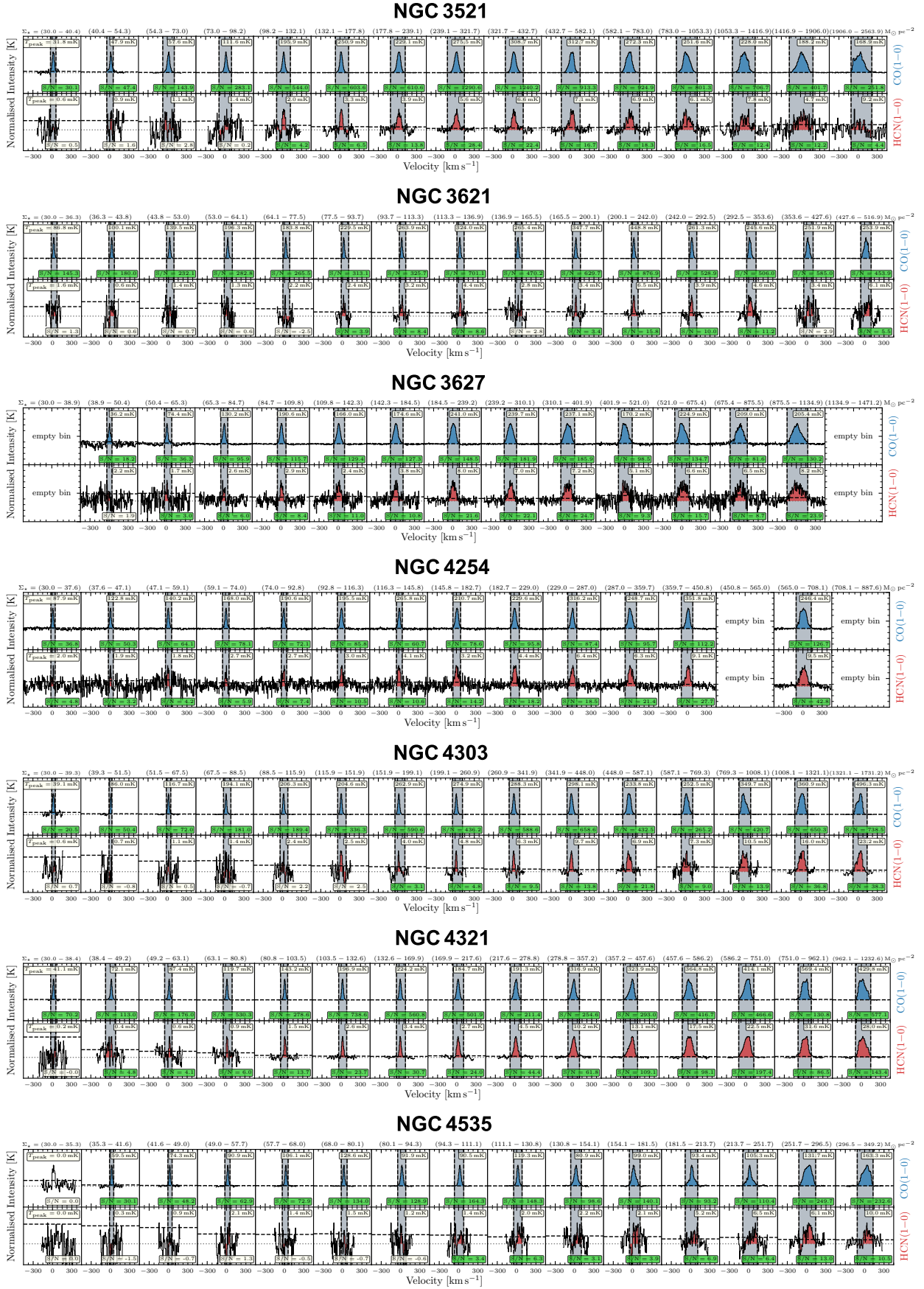
Fig. D.2. Continuation of Fig. D.1.

NGC 3521

NGC 3621

NGC 3627

NGC 4254

NGC 4303

NGC 4321

NGC 4535

Fig. D.3. Continuation of Fig. D.1.

Fig. D.4. Continuation of Fig. D.1.

NGC 6300
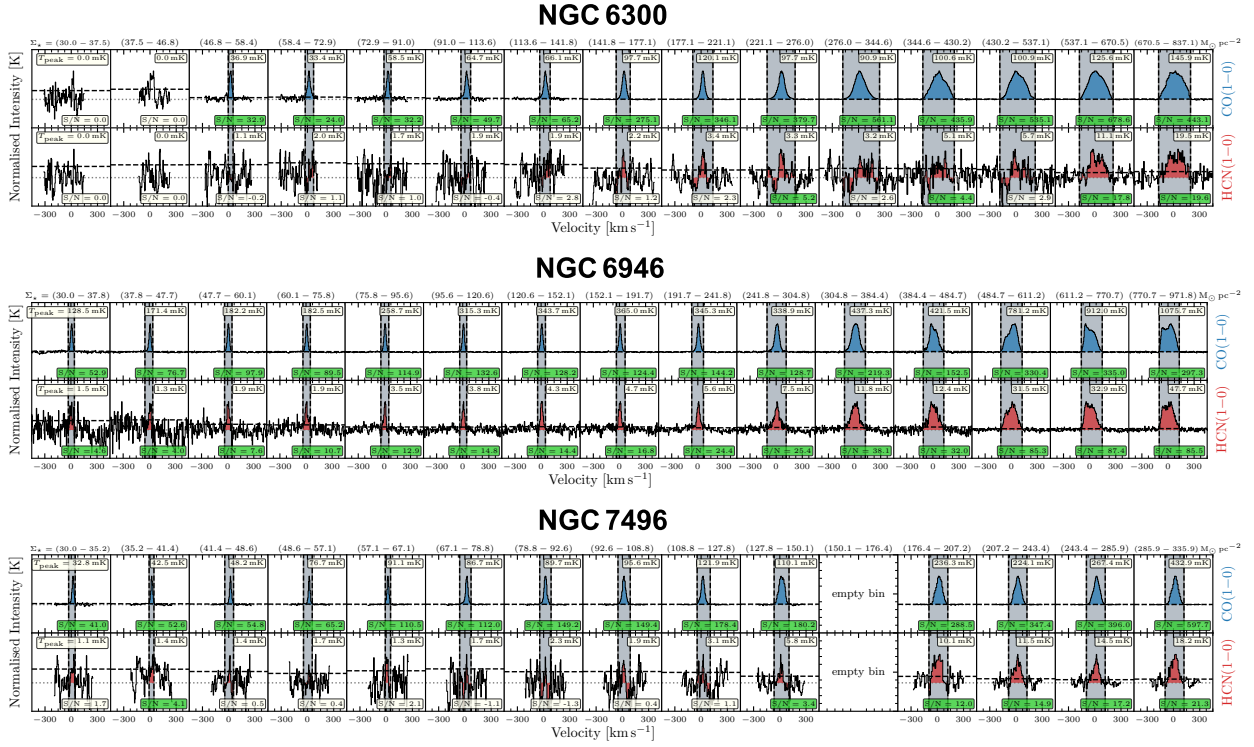

NGC 6946

NGC 7496
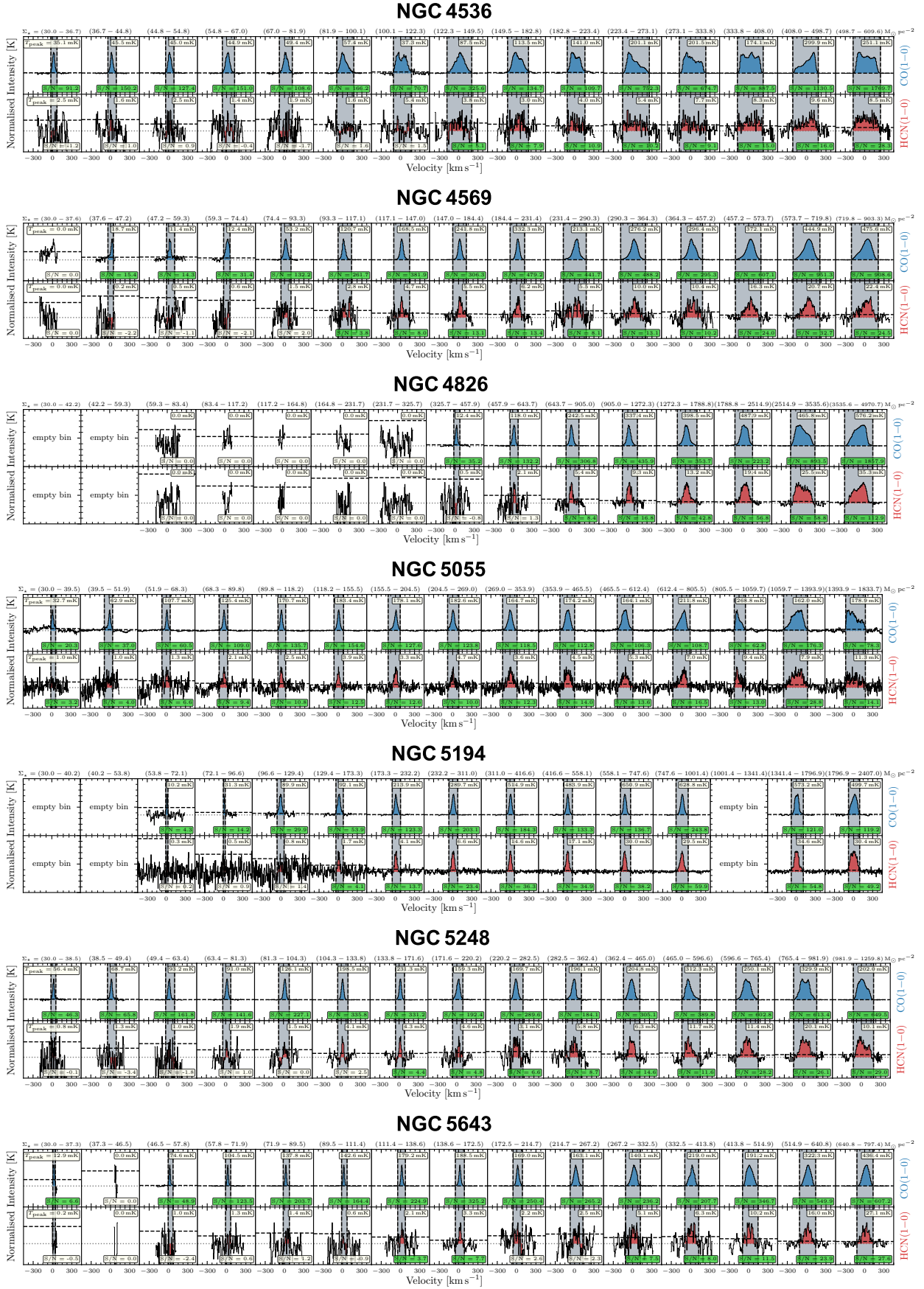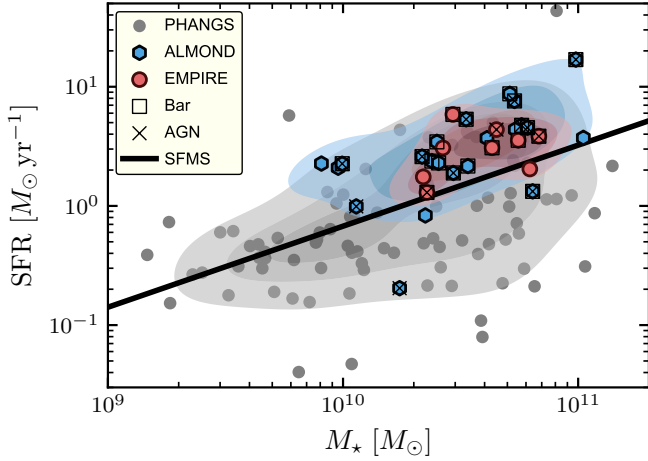

Fig. D.5. Continuation of Fig. D.1.

Fig. E.1. ALMOND and EMPIRE on the star-forming main sequence (SFMS) of galaxies. Grey shows all galaxies from the PHANGS–ALMA survey (Leroy et al. 2021b). Red and blue markers present galaxies from the EMPIRE (Jiménez-Donaire et al. 2019) and ALMOND surveys (Neumann et al. 2023b), respectively, used in this work. Contours indicate 25, 50 and 75 percentile areas of the respective samples. The black solid line marks the star-forming main sequence from z0MGS (Leroy et al. 2019). The black squares and crosses indicate the presence of a bar or active galactic nucleus (AGN) in the respective galaxy, taken from Tab. E.1.